nature photonics

Supplementary information https://doi.org/10.1038/s41566-024-01506-y

Perovskite computed tomography imager and three-dimensional reconstruction

In the format provided by the authors and unedited

Table of Contents:

Supplementary Figures 1-13

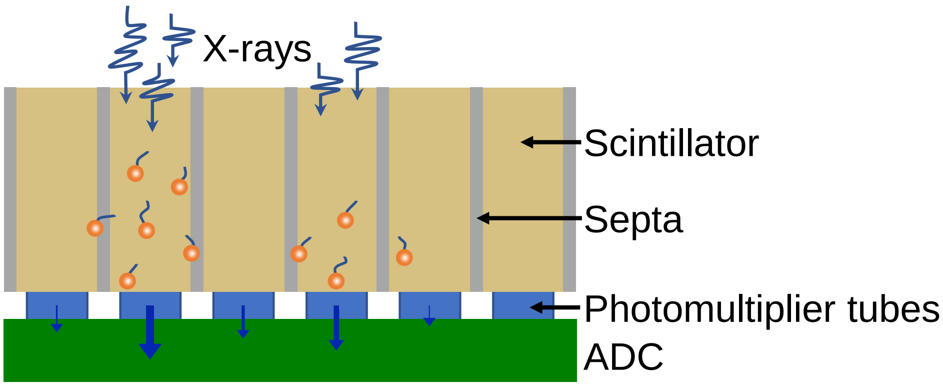

Supplementary Fig. 1 | The working mechanism of scintillator X-ray detector in indirect detection mode. Scintillators produce photons when exposed to X-rays, corresponding to the energy absorbed from the X-rays. Yet, these photons can scatter and attenuate within the scintillator, compromising image quality. When converting these photons to electronic signals, septa are used to prevent cross-talk between photodiodes, but they might absorb some photons, diminishing image contrast and sensitivity. Hence, scintillator-based indirect detectors, with intricate photon pathways and multiple energy conversions, can face challenges in producing optimal images.

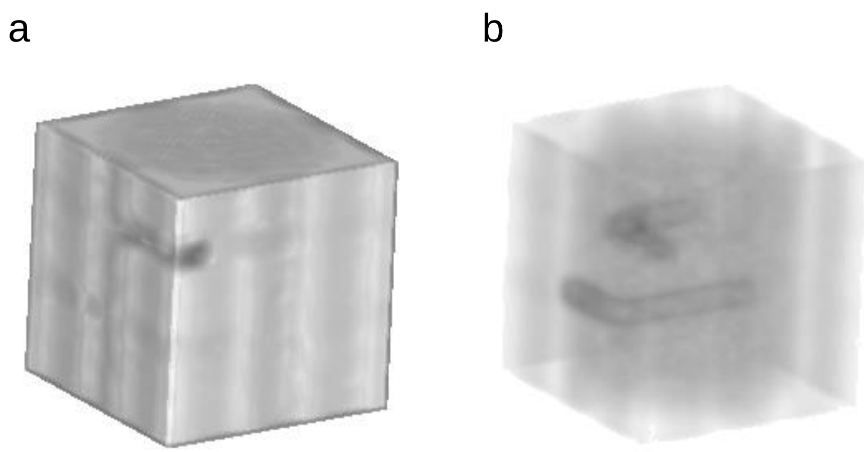

Supplementary Fig. 2 | 3D reconstruction of the cube. a, The initial 3D reconstruction of the cube. **b,** Internal channel visualization in 3D model. The 3D model in Supplementary Fig. 2a shows exterior form of the cube. In Supplementary Fig. 2b, adjusting the model's opacity reveals internal channels, underscoring CT's capability to visualize the interior of objects.

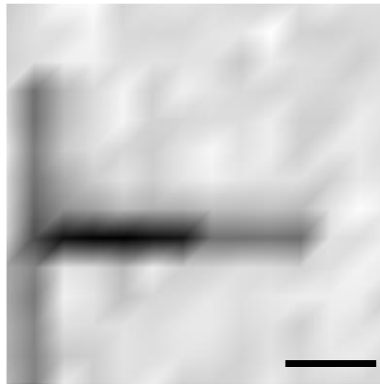

Supplementary Fig. 3 | Planar X-ray image of the cube. The planar X-ray image, depicting the same object as in Supplementary Fig. 2. The overlapping data from tubes at different heights blurs the actual interior, complicating image interpretation and potentially masking important details. The red black bar is 5 mm.

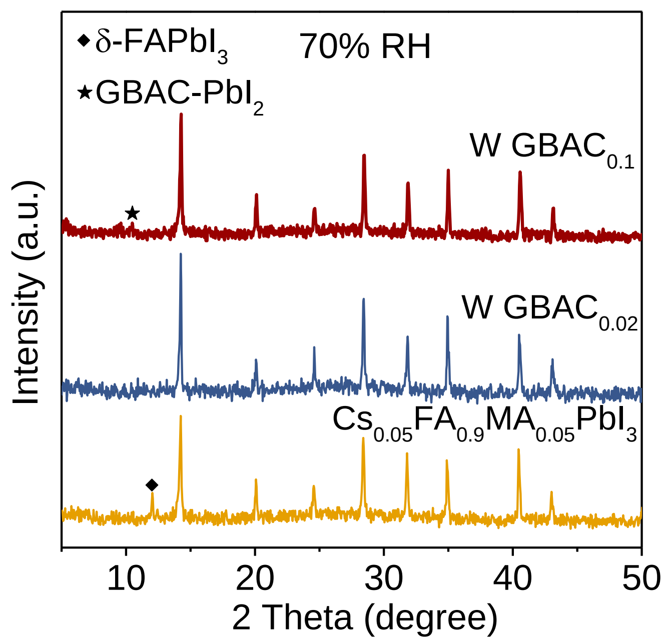

Supplementary Fig. 4 | XRD spectra of $Cs_{0.05}FA_{0.9}MA_{0.05}PbI_3$ film with and without GBAC additive. The $Cs_{0.05}FA_{0.9}MA_{0.05}PbI_3$ film was prepared under ambient conditions, revealing the characteristic peaks of the XRD spectrum for the less photosensitive δ-$FAPbI_3$ phase. The incorporation of GBAC effectively suppresses the undesired δ-$FAPbI_3$ phase. However, when the GBAC content increases to 10 mol%, GBAC-PbI_2 structures become apparent, suggesting that excess GBAC is not solely confined to the grain boundaries but interacts more broadly with the material's structure.

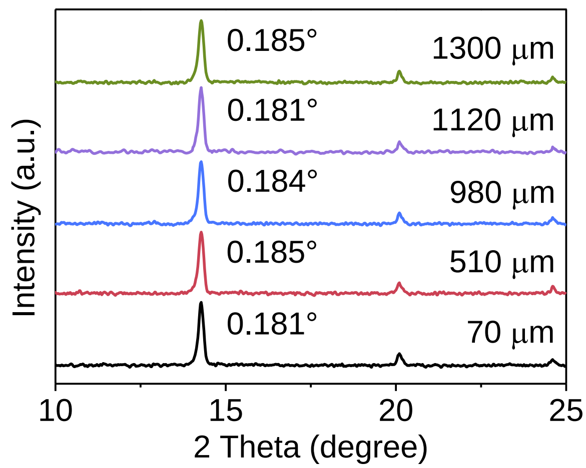

Supplementary Fig. 5 | XRD spectra of films at various thicknesses. The consistent crystal quality across films of varying thickness is indicated by the nearly identical full width at half maximum (FWHM) values.

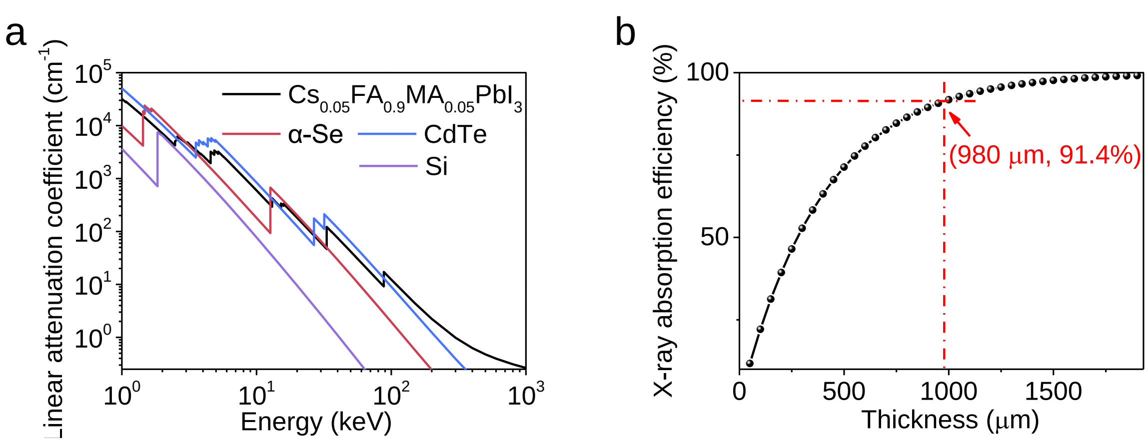

Supplementary Fig. 6 | X-ray absorption properties of a perovskite film. a, Linear attenuation coefficient of Si, CdTe, α-Se, and $Cs_{0.05}FA_{0.9}MA_{0.05}PbI_3$. **b,** X-ray absorption efficiency of $Cs_{0.05}FA_{0.9}MA_{0.05}PbI_3$ at at an X-ray energy of 59.3 keV.

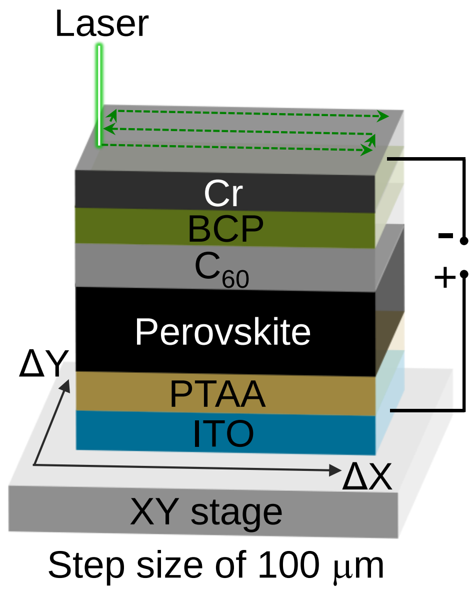

Supplementary Fig. 7 | Schematic of the photodetector configuration and photocurrent test setup. The photodetector structure is comprised of multiple layers including ITO, PTAA, Perovskite, C_{60}, BCP, and Cr. For photocurrent mapping, we employed an X-Y platform to systematically move the device across a 4 mm × 4 mm area, spanning 40 × 40 steps, each step being 100 μm. Different positions on the device were sequentially illuminated by a focused 532 nm laser. At each position, the current was recorded, resulting in a comprehensive current mapping.

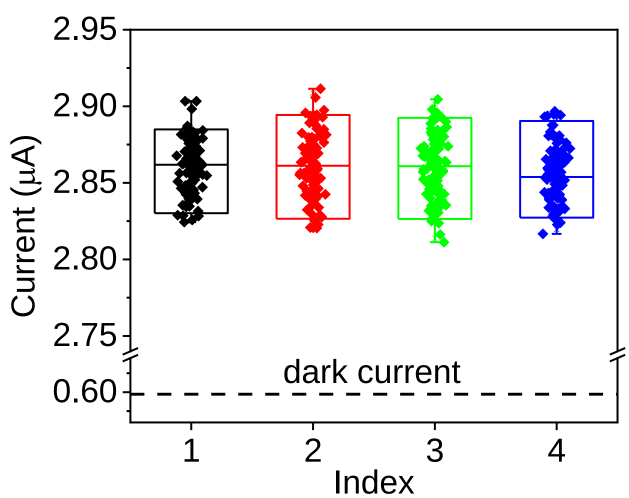

Supplementary Fig. 8 | Photocurrent Mapping Consistency Across the Same Device. Photocurrent measurements at four different time points, each derived from a statistical analysis of 100 data points, demonstrate consistent film performance with minimal deviation in current values across the same device. Each box plot illustrates the distribution, with whiskers representing the minimum and maximum observed values (minimums: 2.824, 2.821, 2.811, 2.817; maximums: 2.903, 2.911, 2.904, 2.896). Boxes span from the 10th percentile (2.837, 2.834, 2.833, 2.832) to the 90th percentile (2.882, 2.891, 2.886, 2.881), with the median marked by the center line at values (2.862, 2.861, 2.860, 2.854).

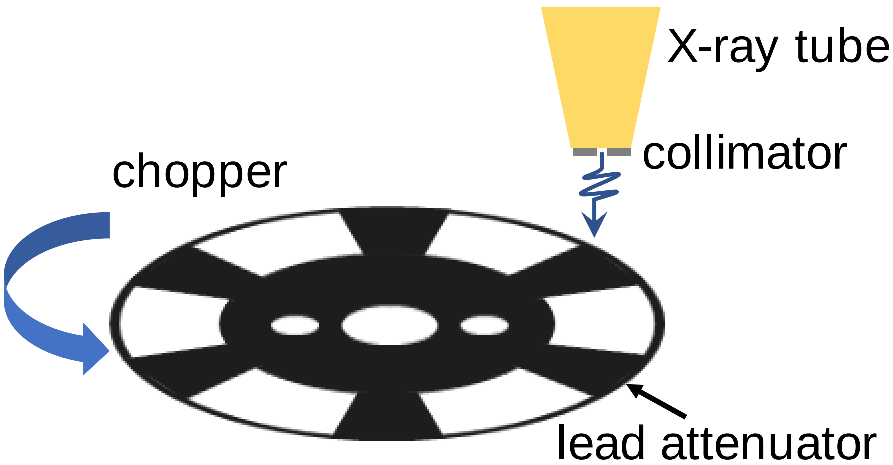

Supplementary Fig. 9 | Schematic of the setup for modulating X-rays into a periodic exposure pattern.

Supplementary Fig. 10 | Photograph of the tooth used for CT imaging.

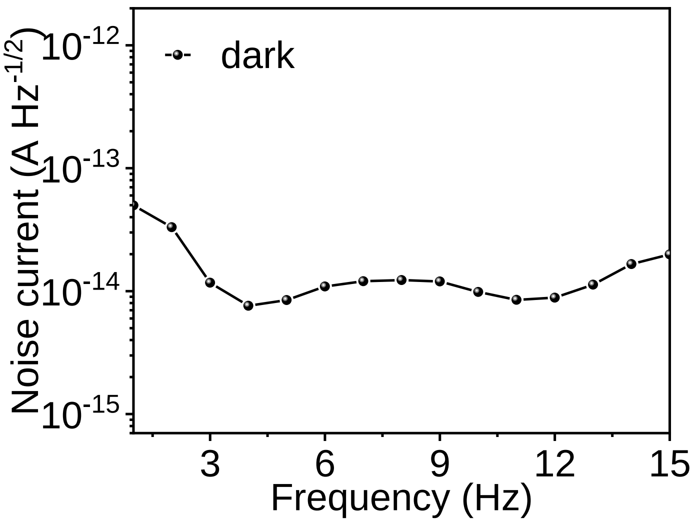

Supplementary Fig. 11 | Detector's noise spectrum at zero dose.

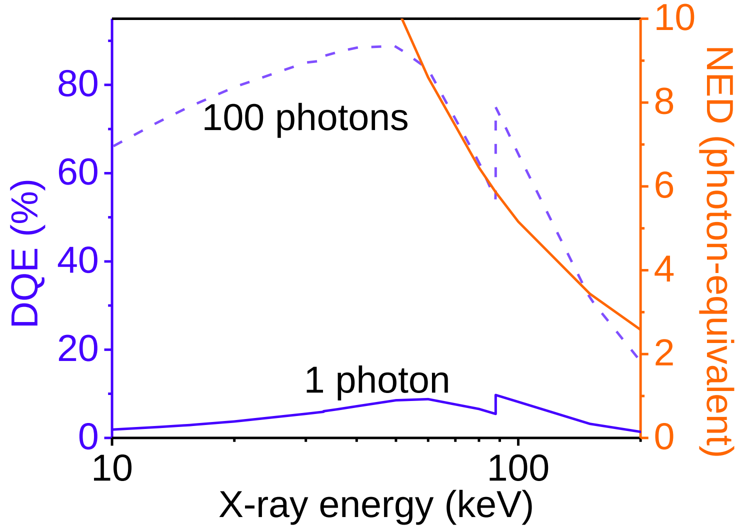

Supplementary Fig. 12 | NED (yellow line) and DQE (blue lines) versus photon energy, calculated from the experimental DE and NED.

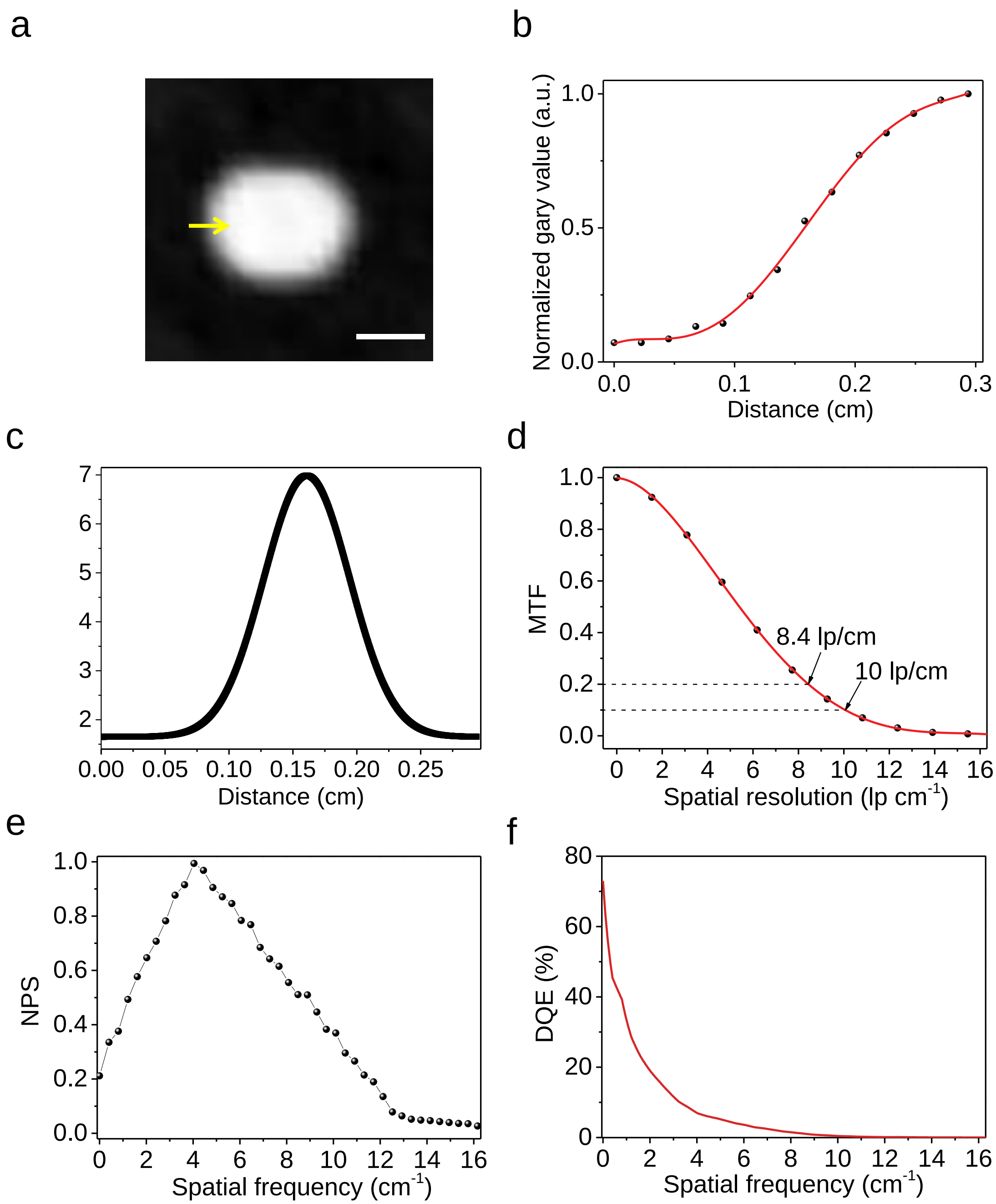

Supplementary Fig. 13 | Analysis of spatial resolution using MTF. a, Reconstructed tooth cervix image highlighting the chosen slanted edge for analysis (indicated by the yellow line). The white scale bar is 5 mm. **b,** 1D edge profile function curve. **c,** LSF curve derived from the 1D edge profile function. **d,** MTF curve derived from the LSF. **e,** Noise power spectrum (NPS) derived from the ROI of reconstructed image. **f,** DQE- spatial frequency curve derived from the folloing formula:

$$\mathrm{DQE}(\upsilon) = \mathrm{DQE}(0) \times \frac{MTF_{(\upsilon)}{}^{2}}{NPS_{(\upsilon)}}.$$

Supplementary Tables 1-2

Supplementary Table. 1 | Comparison of direct conversion X-ray detectors using different perovskite thin/thick films.

Materials	Thickness (μm)	Dark current (mA cm^{-2})	Sensitivity (μC Gy^{-1} cm^{-2})	Reference
$CsPbI_2Br$	40	0.32 (5 V)	148 000	1
$CsPbBr_3$	240	-	55 684	2
$(BA_2PbBr_4)_{0.5}FAPbI_3$	6	10^{-6} (-1 V)	13 600	3
$MAPbI_3$	830	10^{-4} (50 V)	11	4
$Cs_{0.15}FA_{0.85}PbI_3$	520	7×10^{-7} (-25 V)	1 629	5
$MA_{0.42}FA_{0.58}PbI_3$	70	0.54 (-5 V)	1 160 000	6
$MAPbI_3$	60	10^{-3} (80 V)	150	7
$CsPbBr_3$	35	1.5×10^{-6} (-4 V)	2 930	8
$CsPbBr_3$	100	1.4×10^{-3} (120 V)	1 450	9
Cs_2TeI_6	1.5	3.5×10^{-6} (10 V)	226.8	10
$FA_{0.83}Cs_{0.17}PbI_{2.7}Br_{0.3}$	9.2	1.5×10^{-4} (-0.5 V)	3 370.8	11
$BA_2MA_2Pb_3I_{10}$	10	1×10^{-5} (3 V)	1 214	12
$CsPbBr_3$	-	3×10^{-9} (0 V)	470	13
$CsPbBr_3$	110	2.8×10^{-4} (5 V)	11 840	14
$Cs_{0.05}FA_{0.9}MA_{0.05}PbI_3$	980	5×10^{-4} (-200 V)	15 000	This work

Supplementary Table. 2 | Comparison of the perovskite CT system with commercial CT Scanners.

Manufacturer model number	Effective dose; region	Spatial resolution (lp/cm)	Pixel size	Reference
Discovery 710 (GE Healthcare)	5-26 mSv; (-)	1.1 (FWHM)	4.2-6.3 mm	16, 17
Revolution GSI (GE Healthcare)	0.5-12 mGy; liver	5.5-7.5 (MTF=0.1)	1 mm	18
Ingenuity elite (Philips)	5.6 mGy; body	13 (MTF=0.1)	0.797 mm	19
Aquilion Prime (Canon)	3.17-11.4 mSv; chest	8-9 (MTF=0.1)	0.5 mm	20
i-CAT FLX (Imaging Sciences)	0.011-0.12 mSv; CBCT	11.6 (MTF=0.1)	0.125-0.4 mm	21
Galileos (Sirona)	0.203 mSv; CBCT	8.8-8.9 (MTF=0.1)	0.3 mm	22, 23
3D Accuitomo 170 (J. Morita MFG Corp)	0.166 mSv; CBCT	8 (MTF=0.1)	0.12 mm	24
Promax 3D (Planmeca)	0.674 mSv; CBCT	5 (MTF=0.1)	0.14 mm	24
Scanora 3D (Soredex)	0.094 mSv; CBCT	4 (MTF=0.1)	0.13 mm	24
Aquilion Precision (Canon)	15.9-22.3 mGy; body 58.5-69.5 mGy; head	15 (MTF=0.1)	0.25 mm	25

SOMATOM Force (Siemens Healthineers)	3.6 mGy; lung	10.21 (MTF=0.02)	0.45-0.51 mm	26
NAEOTOM Alpha (Siemens Healthineers)	2.7 mGy; lung	11.7 (MTF=0.02)	0.15-0.18 mm	26
iCT (Philips Healthcare)	7 mGy; lung	9.8-10.1 (MTF=0.1)	1.14-1.4 mm	27
Preclinical SPCCT scanner based on Brilliance iCT (Philips Healthcare)	-	21.7 (MTF=0.1)	0.5 mm	27
Perovskite	0.0055 mSv; tooth 0.16 mSv; jaw	10 (MTF=0.1)	0.8 mm	This work

Reference

1. Qian, W., *et al.* An aerosol-liquid-solid process for the general synthesis of halide perovskite thick films for direct-conversion X-ray detectors. *Matter* **4**, 942-954 (2021).

2. Pan, W., *et al.* Hot-Pressed CsPbBr3 Quasi-Monocrystalline Film for Sensitive Direct X-ray Detection. *Adv Mater* **31**, e1904405 (2019).

3. Peng, J., *et al.* Ion-exchange-induced slow crystallization of 2D-3D perovskite thick junctions for X-ray detection and imaging. *Matter* **5**, 2251-2264 (2022).

4. Kim, Y. C., *et al.* Printable organometallic perovskite enables large-area, low-dose X-ray imaging. *Nature* **550**, 87-91 (2017).

5. Ying Zhou, L. Z., Zhenyi Ni, Shuang Xu, Jingjing Zhao, Xun Xiao, Jinsong Huang. Heterojunction structures for reduced noise in large-area and sensitive perovskite x-ray detectors. *Sci Adv* **7**, eabg6716 (2021).

6. Li, W. G., Wang, X. D., Huang, Y. H., Kuang, D. B. Ultrasound-Assisted Crystallization Enables Large-Area Perovskite Quasi-Monocrystalline Film for High-Sensitive X-ray Detection and Imaging. *Adv Mater*, e2210878 (2023).

7. Yakunin, S., *et al.* Detection of X-ray photons by solution-processed organic-inorganic perovskites. *Nat Photonics* **9**, 444-449 (2015).

8. Li, L., Fang, Y., Yang, D. Interlayer-Assisted Growth of Si-Based All-Inorganic Perovskite Films via Chemical Vapor Deposition for Sensitive and Stable X-ray Detection. *J Phys Chem Lett* **13**, 5441-5450 (2022).

9. Matt, G. J., *et al.* Sensitive Direct Converting X‐Ray Detectors Utilizing Crystalline CsPbBr3 Perovskite Films Fabricated via Scalable Melt Processing. *Advanced Materials Interfaces* **7** (2020).

10. Guo, J., *et al.* Oriented preparation of Large-Area uniform Cs(2)TeI(6) perovskite film for high performance X-ray detector. *J Colloid Interface Sci* **624**, 629-636 (2022).

11. Jia, Z., *et al.* High-performance metal halide perovskite X-ray detectors fabricated with antisolvent-assisted spray-coating. *Journal of Alloys and Compounds* **960** (2023).

12. Tsai, H., *et al.* Quasi-2D Perovskite Crystalline Layers for Printable Direct Conversion X-Ray Imaging. *Adv Mater* **34**, e2106498 (2022).

13. Gou, Z., *et al.* Self‐Powered X‐Ray Detector Based on All‐Inorganic Perovskite Thick Film with High Sensitivity Under Low Dose Rate. *physica status solidi (RRL) – Rapid Research Letters* **13** (2019).

14. Haruta, Y., Ikenoue, T., Miyake, M., Hirato, T. Fabrication of CsPbBr3 Thick Films by Using a Mist Deposition Method for Highly Sensitive X-ray Detection. *MRS Advances* **5**, 395-401 (2020).

15. Barca, P., Giannelli, M., Fantacci, M. E., Caramella, D. Computed tomography imaging with the Adaptive Statistical Iterative Reconstruction (ASIR) algorithm: dependence of image quality on the blending level of reconstruction. *Australas Phys Eng Sci Med* **41**, 463-473 (2018).

16. Alkhorayef, M. Effective radiation doses in pediatric PET/CT examinations: Pilot study. *Appl Radiat Isot* **168**, 109412 (2021).

17. Wagatsuma, K., *et al.* Direct comparison of brain [(18)F]FDG images acquired by SiPM-based and PMT-based PET/CT: phantom and clinical studies. *EJNMMI Phys* **7**, 70 (2020).

18. Greffier, J., *et al.* CT iterative reconstruction algorithms: a task-based image quality assessment. *Eur Radiol* **30**, 487-500 (2020).

19. Narita, A., Ohkubo, M., Fukaya, T., Noto, Y. Method for determining slice sensitivity profile of iterative reconstruction CT images using low-contrast sphere phantom. *Radiol Phys Technol* **14**, 366-372 (2021).

20. Ito, T., *et al.* Verification of phantom accuracy using a Monte Carlo simulation: bone scintigraphy chest phantom. *Radiol Phys Technol* **14**, 336-344 (2021).

21. Ludlow, J. B., Walker, C. Assessment of phantom dosimetry and image quality of i-CAT FLX cone-beam computed tomography. *Am J Orthod Dentofacial Orthop* **144**, 802-817 (2013).

22. Steiding, C., Kolditz, D., Kalender, W. A. A quality assurance framework for the fully automated and objective evaluation of image quality in cone-beam computed tomography. *Med Phys* **41**, 031901 (2014).

23. Qiang, W., Qiang, F., Lin, L. Estimation of Effective Dose of Dental X-Ray Devices. *Radiat Prot Dosimetry* **183**, 417-421 (2019).

24. Suomalainen, A., *et al.* Dosimetry and image quality of four dental cone beam computed tomography scanners compared with multislice computed tomography scanners. *Dentomaxillofac Radiol* **38**, 367-378 (2009).

25. Boedeker, K. Aquilion precision ultra-high resolution CT: quantifying diagnostic image quality. 2017 [cited 2023]; Canon Medical Systems Corporation:[Available from: https://global.medical.canon/publication/ct/2018WP_Aquilion_Precision_Ultra-High_Resolution

26. Gaillandre, Y., *et al.* Ultra-high resolution CT imaging of interstitial lung disease: impact of photon-counting CT in 112 patients. *Eur Radiol* **33**, 5528-5539 (2023).

27. Kopp, F. K., *et al.* Evaluation of a preclinical photon-counting CT prototype for pulmonary imaging. *Sci Rep* **8**, 17386 (2018).